Model-data comparisons of shear waves in the nearshore

T. James Noyes, R. T. Guza, and Falk Feddersen
Integrative Oceanography Division, Scripps Institution of Oceanography, La Jolla, California, USA

Steve Elgar
Woods Hole Oceanographic Institution, Woods Hole, Massachusetts, USA

T. H. C. Herbers
Department of Oceanography, Naval Postgraduate School, Monterey, California, USA

Received 20 June 2004; revised 17 February 2005; accepted 16 March 2005; published 27 May 2005.

[1] Observations of shear waves, alongshore propagating meanders of the mean alongshore current with periods of a few minutes and alongshore wavelengths of a few hundred meters, are compared with model predictions based on numerical solutions of the nonlinear shallow water equations. The model (after Özkan-Haller and Kirby (1999)) assumes alongshore homogeneity and temporally steady wave forcing and neglects wave-current interactions, eddy mixing, and spatial variation of the (nonlinear) bottom drag coefficient. Although the shapes of observed and modeled shear wave velocity spectra differ, and root-mean-square velocity fluctuations agree only to within a factor of about 3, aspects of the cross-shore structure of the observed ($\sim$0.5–1.0 m above the seafloor) and modeled (vertically integrated) shear waves are qualitatively similar. Within the surf zone, where the mean alongshore current (V) is strong and shear waves are energetic, observed and modeled shear wave alongshore phase speeds agree and are close to both V and C_{lin} (the phase speed of linearly unstable modes) consistent with previous results. Farther offshore, where V is weak and observed and modeled shear wave energy levels decay rapidly, modeled and observed C diverge from C_{lin} and are close to the weak alongshore current V. The simulations suggest that the alongshore advection of eddies shed from the strong, sheared flow closer to shore may contribute to the offshore decrease in shear wave phase speeds. Similar to the observations, the modeled cross- and alongshore shear wave velocity fluctuations have approximately equal magnitude, and the modeled vorticity changes sign across the surf zone.

Citation: Noyes, T. J., R. T. Guza, F. Feddersen, S. Elgar, and T. H. C. Herbers (2005), Model-data comparisons of shear waves in the nearshore, *J. Geophys. Res.*, *110*, C05019, doi:10.1029/2004JC002541.

1. Introduction

[2] Shear waves are several-hundred-meter-long, few-minute-period instabilities of the breaking-wave-driven mean alongshore current [*Bowen and Holman*, 1989; *Oltman-Shay et al.*, 1989]. Given the cross-shore (x) profile of the mean alongshore current $V(x)$ and the water depth, linear stability analysis provides the frequencies, wave numbers, initial growth rates, and spatial structure of theoretically unstable modes, but not the modal amplitudes nor their effect on $V(x)$ [e.g., *Dodd et al.*, 1992]. Simulations based on the nonlinear shallow water equations (NSWE) provide complete time histories of the instabilities [*Allen et al.*, 1996; *Slinn et al.*, 1998]. For barely unstable V, the simulations result in weakly nonlinear shear waves with frequency f, alongshore wave number k, and spatial structure that closely resemble the theoretically most rapidly growing mode [*Feddersen*, 1998]. In this case, finite amplitude effects slightly alter $V(x)$ and shear wave properties. More nonlinear shear waves form unsteady, alongshore progressive vortices that occasionally merge. With strongly nonlinear shear waves, eddies are ejected from the surf zone, and shear wave mixing substantially alters $V(x)$, eventually limiting the growth of the instabilities [*Allen et al.*, 1996; *Slinn et al.*, 1998]. Except for the weakest nonlinearity (when shear wave energy is highly concentrated at the k-f of the most unstable mode and its harmonics), the simulated shear wave energy is spread relatively smoothly over a nondispersive wave number–frequency band, with roughly the frequency range of linearly unstable (k, f).

[3] Simulations from a NSWE model agree qualitatively with shear wave phase speeds and energy levels observed with an alongshore array of current meters located about 40 m from the shoreline at Duck, NC [*Özkan-Haller and Kirby*, 1999]. Shear wave linear stability theory and numerical models have been reviewed and compared with

0148-0227/05/2004JC002541$09.00

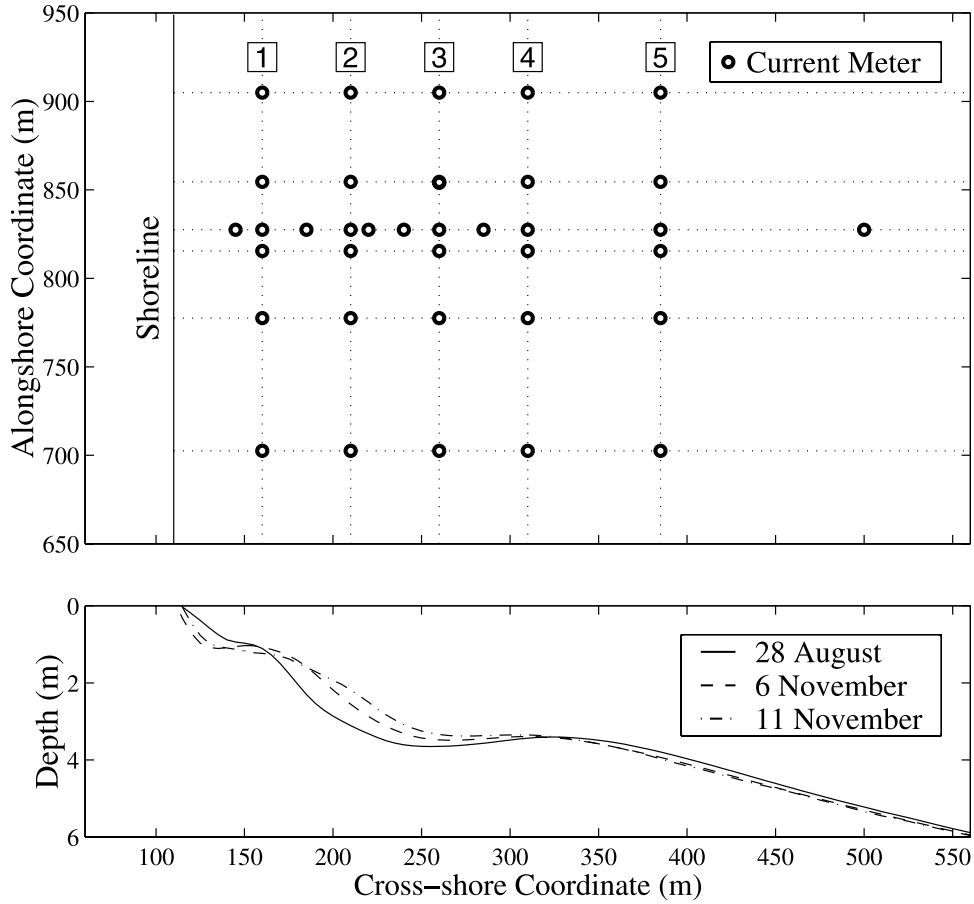

Figure 1. (top) Plan view of instrument array. Each circle indicates a horizontal velocity (u, v) sensor, usually positioned between 0.5 and 1.0 m above the seafloor. The Field Research Facility (located near Duck, North Carolina) coordinate frame is used. Numbers within boxes denote the five alongshore arrays. The approximate location of the shoreline is shown near x = 110 m. (bottom) Alongshore-averaged seafloor elevation (depth below mean sea level) versus cross-shore coordinate (dates in legend).

field observations at a single cross-shore location [*Dodd et al.*, 2000].

[4] Case examples of shear waves observed with five alongshore arrays of current meters spanning the surf zone are described in section 2. Numerical simulations based on NSWE (section 3) suggest that shear wave mixing significantly alters $V(x)$, consistent with previous work. Near the shoreline, the alongshore phase speeds observed, numerically simulated, and predicted by linear stability theory agree within about 30% (section 4). However, farther offshore where V and shear waves are weaker, the observed and modeled alongshore phase speeds are much slower than predicted by linear stability theory, perhaps owing to advection of eddies shed from the stronger flow near the shoreline. The results are summarized in section 5.

2. Observations

[5] Colocated pressure gauges and bidirectional current meters (PUV) were deployed at 11 locations along a cross-shore transect extending from ≈1.0 m depth (≈50 m from the shoreline) to ≈5.5 m depth (≈400 m from the shoreline). At 5 cross-shore locations, a six-element, 200 m aperture alongshore PUV array was deployed (Figure 1). The bathymetry and mean (1 hour averaged) circulation observed at the instrumented locations usually were alongshore homogeneous [*Feddersen and Guza*, 2003], although alongshore variability of V at the shallowest array is significant on 1 November and 13 November (Figures 2b and 2c). Shear waves observed during the 4-month-long SandyDuck experiment are described by *Noyes et al.* [2004].

[6] Observations are compared with numerical model predictions for four, 3-hour-long case examples with different alongshore flows (Figure 2), including a relatively weak (incident wave height H_{rms} = 0.55 m (Table 1), maximum $V_{max} \approx$ 45 cm/s) shoreline-intensified jet with a narrow surf zone (28 August), a stronger (H_{rms} = 1.05 m, $V_{max} \approx$ 100 cm/s) shoreline-intensified jet with a wider surf zone (1 November), and moderate flows ($V_{max} \approx$ 75 cm/s) that are either broad with a wide surf zone (H_{rms} = 1.90 m, 13 November), or more jet-like with a narrower surf zone (H_{rms} = 0.68 m, 17 November, similar to the $V(x)$ examined by *Özkan-Haller and Kirby* [1999]). The wind stress τ^{wind}, estimated from measurements 800 m from the shoreline at the end of the nearby pier, was weak relative to the forcing by breaking waves.

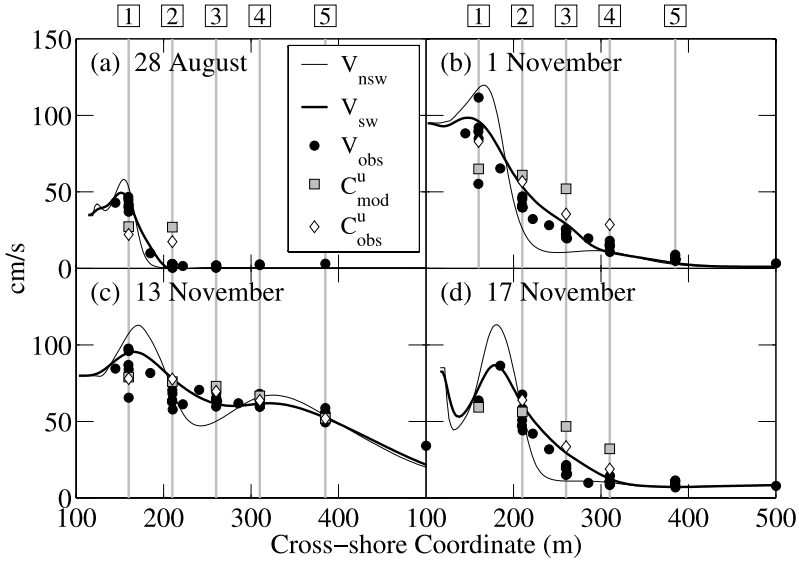

Figure 2. Observed mean alongshore current (V_{obs}, circles), modeled mean alongshore currents with and without mixing by shear wave fluctuations (V_{sw} and V_{nsw}, bold and thin curves, respectively), and observed and modeled shear wave phase speeds ($C_{obs}{}^{u}$ and $C_{mod}{}^{u}$, diamonds and squares, respectively) versus the cross-shore coordinate. On 13 and 17 November, V was directed southward but is plotted here (and elsewhere) with reversed sign for comparison with the other cases. The phase speed C^u equals the slope of the energy-weighted, best-fit line to the shear wave ridge in cross-shore velocity spectra $E^u(k, f)$ (Figures 3–6). Numbers within boxes and vertical shaded lines indicate the positions of operational alongshore arrays (Figure 1). In some cases an array was operational, but shear wave signal levels were too low to estimate $C_{obs}{}^{u}$ (e.g., arrays 3, 4, and 5 on 28 August).

[7] Shear waves appear in wave number–frequency spectra ($E^u(k, f)$ and $E^v(k, f)$, for cross-(u) and alongshore (v) velocity components) as a ridge of elevated energy corresponding to approximately nondispersive (i.e., f varies linearly with k) propagation in the same direction as V [e.g., *Oltman-Shay et al.*, 1989] (Figures 3–7). Wave number–frequency spectra for v are similar to those for u (compare Figure 6 with 7), and results for u are discussed in detail below.

3. Model Description and Calibration

[8] Shear waves were modeled using the time-dependent, vertically integrated, rigid-lid nonlinear shallow water equations (NSWE), averaged over incident wave time-scales, with breaking wave forcing and a quadratic bottom stress (Appendix B). To reduce the number of adjustable coefficients, and because observed and modeled shear wave energies are most similar when eddy mixing is weaker than shear wave mixing [*Özkan-Haller and Kirby*, 1999], lateral mixing from processes other than shear waves is neglected (e.g., an eddy viscosity term is not included). The effects of wave-current interactions [*Özkan-Haller and Li*, 2003], shear dispersion [*Svendsen and Putrevu*, 1994], cross-shore variation of the bottom drag coefficient [*Church and Thornton*, 1993; *Feddersen et al.*, 2004], and temporal variation of V and S_{yx} associated with wave groups [*Haller et al.*, 1999] also are neglected. The only adjustable parameter in this relatively simple model is the bottom drag coefficient c_d. Mean momentum fluxes of incident swell and sea were characterized using radiation stresses estimated with a separate "roller" model, initialized with observations in 8 m depth (Appendix C). Several cross-shore depth profiles spanning the alongshore extent of the current meter arrays were averaged to obtain the cross-shore depth profiles $h(x)$ (Figure 1) used in the simulations. The bottom drag coefficient c_d (B3) for each run (Table 1)

Table 1. Incident Wave Conditions (Integrated Over Frequencies Between 0.05 and 0.30 Hz) Measured in 8 m Water Depth, About 800 m From the Shoreline[a]

Date and Time, LST	H_{rms}, m	S_{yx}/ρ, m^3/s^2	f_m, Hz	θ_{inc}, deg	c_d, $\times 10^{-3}$
28 Aug. 1000	0.55	0.06	0.12	10.1	2.25
1 Nov. 0700	1.05	0.28	0.12	14.6	1.25
13 Nov. 1600	1.90	−0.44	0.14	−7.2	1.00
17 Nov. 0100	0.68	−0.14	0.17	−20.6	1.50

[a]From *Long* [1996]. H_{rms} is the root-mean-square wave height, S_{yx}/ρ is the off-diagonal radiation stress component divided by the water density, f_m is the energy-weighted mean frequency, and θ_{inc} is the incident wave angle defined in Appendix C. The drag coefficient c_d is determined by matching the model and observed maximum V.

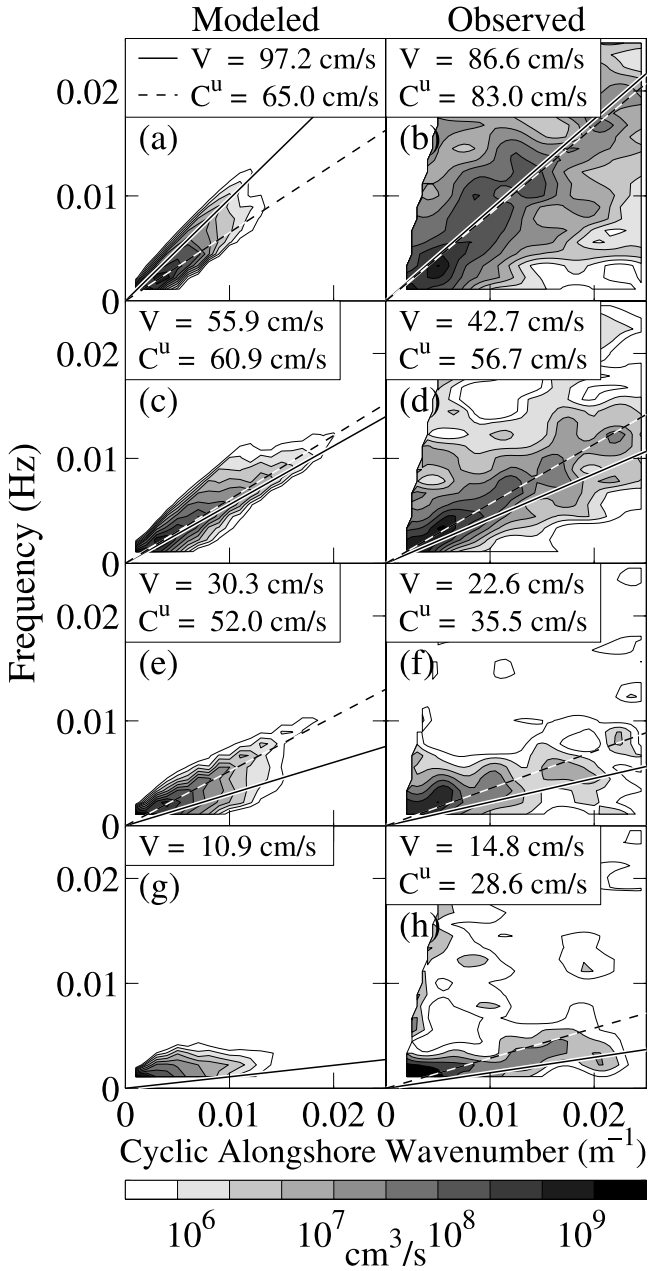

Figure 3. (left) Modeled and (right) observed wave number–frequency spectra of cross-shore velocity $E^u(k, f)$ at arrays (top to bottom) 1, 2, 3, and 4 for 1 November. The logarithmic gray scale for energy density is shown at the figure bottom. Spectra are shown only for k with propagation in the V direction and magnitude greater than the theoretical limit for gravity waves given by the mode 0 edge wave dispersion curve (a small offset of 0.0015 m^{-1} is added to reduce edge wave leakage into the shear wave estimates). The local mean alongshore current V (solid line) and estimated shear wave phase speed C^u (dashed line) are given in the legends. The linear stability predicted shear wave phase speed C_{lin} = 78 cm/s.

was chosen so that the maximum value of the modeled (with shear wave mixing, V_{sw}) mean alongshore current matched the maximum of the observed (V_{obs}) current. The cross-shore structure of $V_{obs}(x)$ usually is reproduced by the model (compare the thick curves with the filled circles in Figure 2). The c_d values ($\approx 10^{-3}$) are similar to those estimated from alongshore momentum balances using many 24-hour-long observations of mean currents obtained between August and November [*Feddersen and Guza*, 2003]. The difference between V modeled with (V_{sw}) and without (V_{nsw}) shear wave fluctuations is significant (compare thick with thin curves in Figure 2), except on 28 August when V is relatively weak. (The alongshore current V_{nsw} is the solution to the temporally steady model equations that are obtained when shear wave fluctuations are set equal to zero.) The numerical accuracy of the model is confirmed by close agreement between simulations (with linear friction and no roller) and analytic solutions for finite amplitude, weakly nonlinear shear waves [*Feddersen*, 1998]. Results for alongshore domain lengths L_y of 1000, 1500, and (for one case) 1600 m differed in detail, but were qualitatively similar (e.g., energy was similarly concentrated in k-f space). Results are shown for L_y = 1000 m.

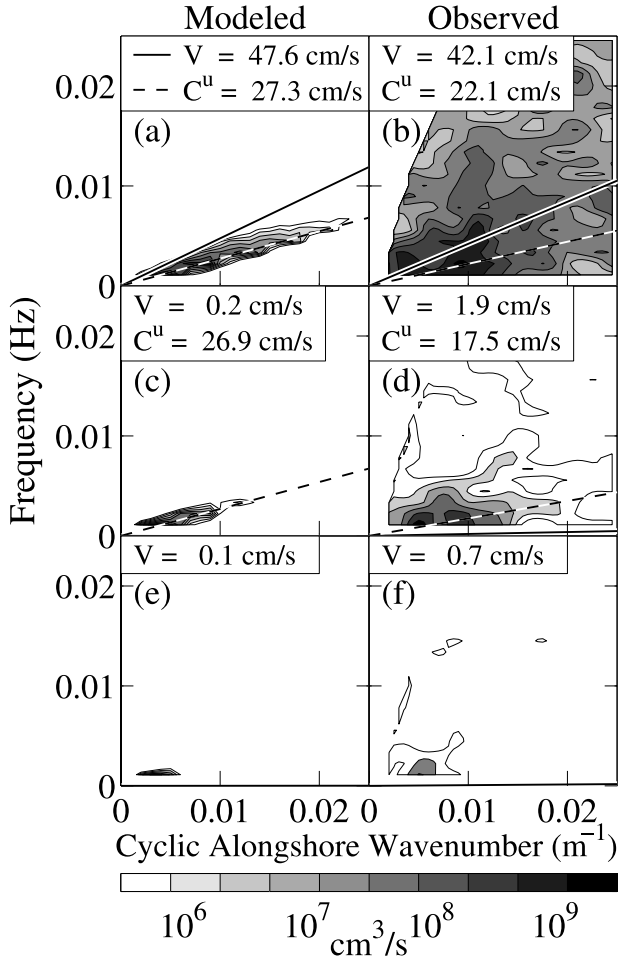

Figure 4. (left) Modeled and (right) observed wave number–frequency spectra of cross-shore velocity $E^u(k, f)$ at arrays (top to bottom) 1, 2, and 3 for 28 August. The format is the same as Figure 3. A ridge was not present in the modeled or observed $E(k, f)$ at array 3, so C^u is not estimated. C_{lin} = 34 cm/s.

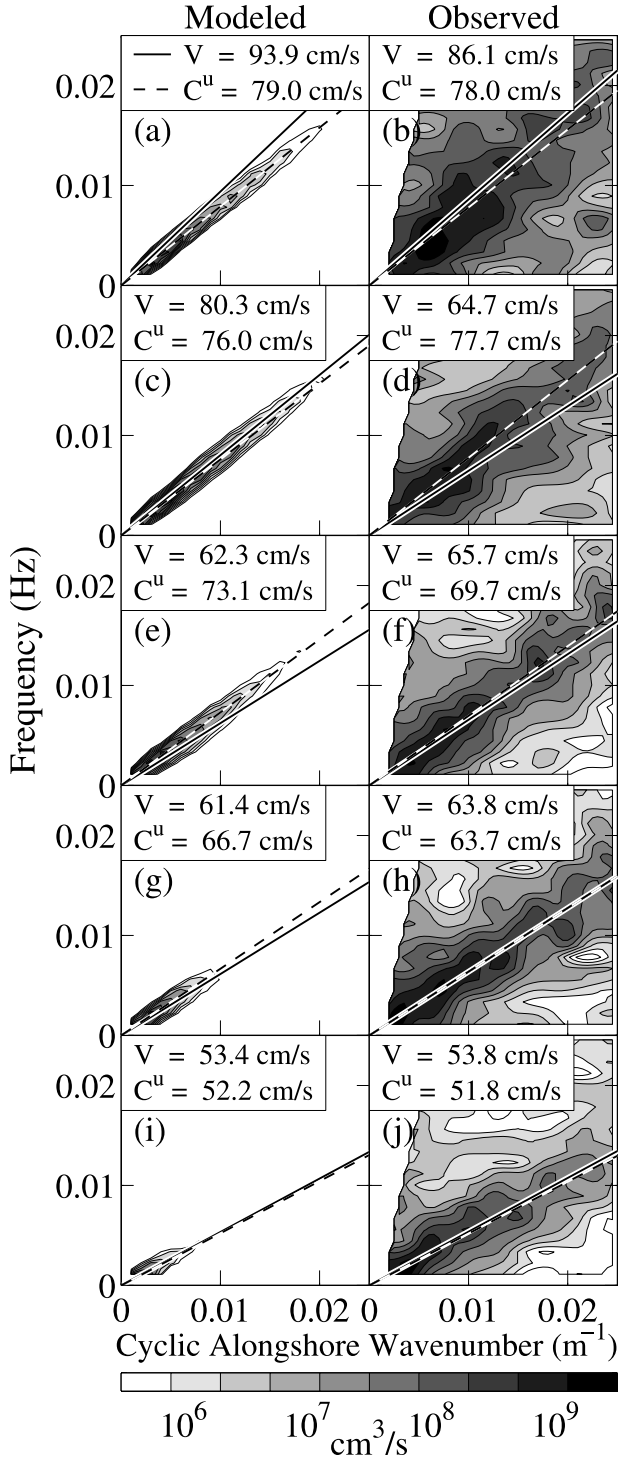

Figure 5. (left) Modeled and (right) observed wave number–frequency spectra of cross-shore velocity $E^u(k, f)$ at arrays (top to bottom) 1, 2, 3, 4, and 5 for 13 November. The format is the same as Figure 3. The V and C^u were directed southward but are plotted as if directed northward for comparison with other cases. C_{lin} = 82 cm/s.

[9] Modeled instantaneous vorticity fields on 28 August do not show eddy formation, consistent with weakly nonlinear shear waves [*Allen et al.*, 1996]. Vortices form in the other 3 case examples (1 November is shown in Figure 8), indicating that the modeled shear waves are more nonlinear than on 28 August.

4. Comparison of Observations With Numerical Simulations

4.1. Alongshore Phase Speeds

[10] Nondispersive shear wave phase speeds C^u and C^v were estimated from the slope of the energy-weighted best-fit line to the shear wave ridge in $E^u(k, f)$ and $E^v(k, f)$, respectively ($E^u(k, f)$ and C^u are shown in Figures 3–6). Estimates of C^u and C^v often are dominated by the lowest frequencies, which usually have the highest shear wave energy. In a few cases a ridge was judged subjectively to be absent in either the observed or modeled $E(k, f)$ (e.g., Figures 4e and 4f), and the corresponding C value was discarded. In both the observations [*Noyes et al.*, 2004] and the simulations (not shown) $C^u \approx C^v$.

[11] On 28 August, the case with the weakest V, the model $C^u_{mod} \approx 27$ cm/s at arrays 1 and 2 (the only cross-shore locations where C_{mod} could be determined, Figures 4a

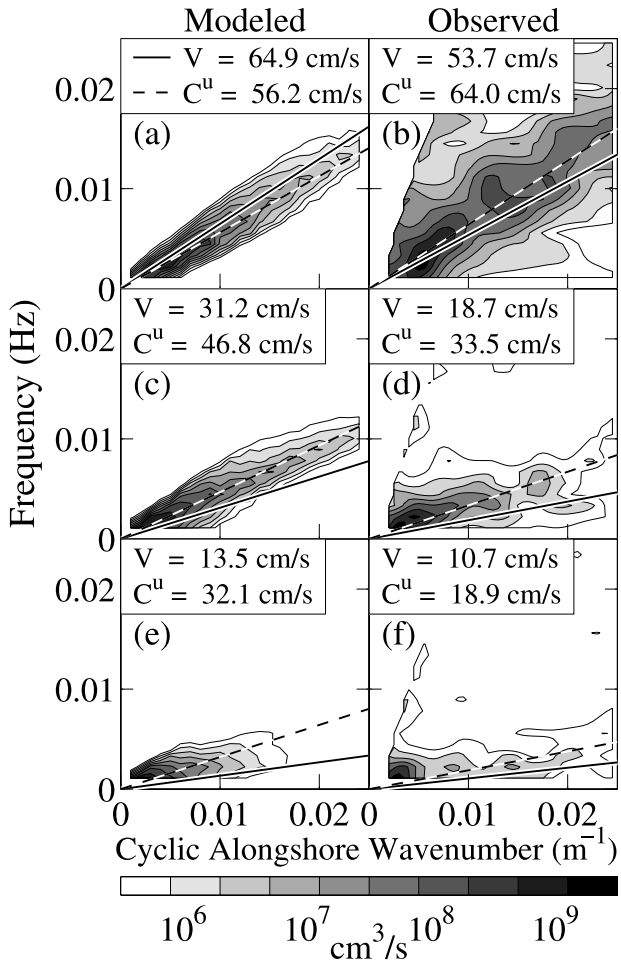

Figure 6. (left) Modeled and (right) observed wave number–frequency spectra of cross-shore velocity $E^u(k, f)$ at arrays (top to bottom) 2, 3, and 4 for 17 November. The format is the same as Figure 3. The observed V and C^u were directed southward but are plotted as if directed northward for comparison with other cases. C_{lin} = 60 cm/s.

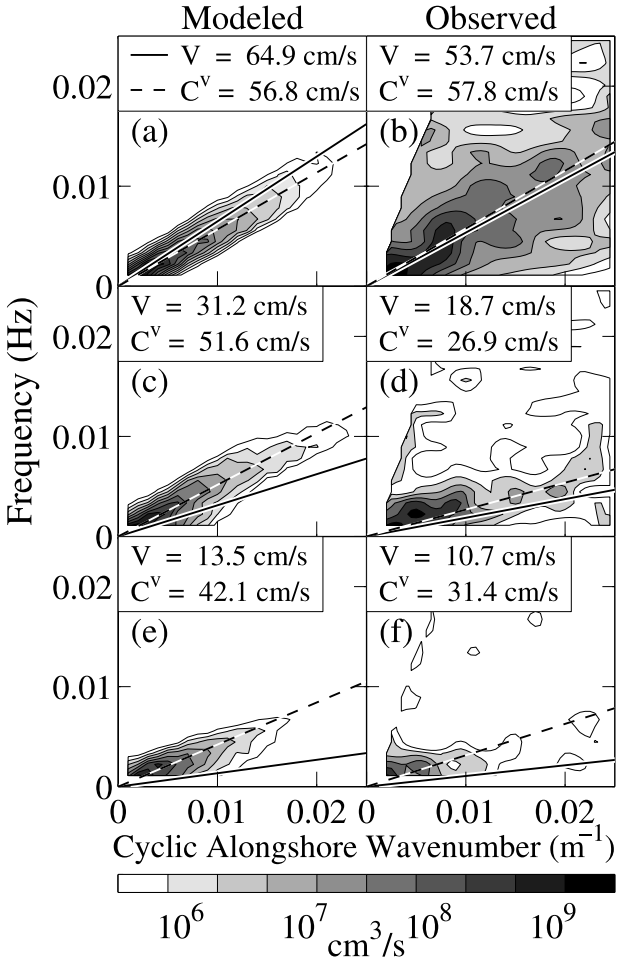

Figure 7. (left) Modeled and (right) observed wave number–frequency spectra of alongshore-shore velocity $E^v(k, f)$ at arrays (top to bottom) 2, 3, and 4 for 17 November. The format is the same as Figure 3, except here for v rather than u. The observed V and C^v were directed southward but are plotted as if directed northward for comparison with other cases. C_{lin} = 60 cm/s.

and 4c, and filled squares in Figure 2a). The model phase speed C^u_{mod} is about 20% less than the phase speed of the fastest growing linear mode C_{lin} = 34 cm/s. (The phase speed C_{lin} for a single linearly unstable mode is a function only of f and k, and thus is constant in the cross shore.) On 28 August, shear wave mixing is weak and C_{lin} of the model mean alongshore currents with (V_{sw}) or without (V_{nsw}) shear waves are similar.

[12] With larger incident waves and increased radiation stress S_{yx} (Table 1), V is stronger and broader (Figures 2b–2d), and shear waves (i.e., ridges of energy in k-f spectra) can be detected farther offshore in both the observations and the model simulations. Observed and modeled C and V near the shoreline (e.g., arrays 1 and 2) usually are within 30% of the phase speed of the most rapidly growing linear modes (Figures 3–6), similar to *Allen et al.* [1996] and *Özkan-Haller and Kirby* [1999]. In contrast to the cross-shore constant C_{lin}, C_{mod} and (especially) C_{obs} decrease offshore where V is smaller and shear wave energies are much reduced (Figures 2b–2d).

[13] Successive contour maps of the modeled spatial distribution of vorticity (e.g., Figure 8) and time-space trajectories of vorticity (Figure 9) [after *Özkan-Haller and Kirby*, 1999] at array 3 on 1 November show the simultaneous presence of features with different phase speeds. Vorticity fronts propagate with alongshore phase speed $C \approx 60$ cm/s, approximately equal to the modeled C based on ridges in $E(k, f)$ spectra (C^u_{mod} = 52 cm/s in Figure 3e) whereas eddies shed intermittently from the vorticity front propagate more slowly. The eddy alongshore propagation speed (≈40 cm/s, estimated from the slope of the light blue ridges in Figure 9) at array 3 is closer to the modeled local mean V (≈29 cm/s) than to the speed of the vorticity front (≈60 cm/s). Model $E(k, f)$ are broadened by the eddies. Vorticity fronts that dominate near the shoreline do not reach as far offshore as array 4, and time-space trajectories of vorticity more than about 300 m from the shoreline are dominated by eddies (not shown).

[14] The shear wave phase speeds estimated from observations (C^u_{obs}) and predicted by the nonlinear model (C^u_{mod}) agree fairly well for all 4 cases (Figure 10a). In contrast to the cross-shore constant $C = C_{lin}$ expected for weakly nonlinear shear waves (e.g., 28 August, no eddy formation), C^u_{obs} and C^u_{mod} usually decrease from values close to C_{lin} within the alongshore current jet near the shoreline to smaller values close to V offshore (Figure 10b). On 28 August the observed and numerically modeled shear wave energy levels offshore of array 2 were too weak to estimate C reliably. In the other three cases, C^u_{obs} is close to the local alongshore current V_{obs} at all array locations, with similar, but weaker cross-shore variation of C^u_{mod} (diamonds and squares respectively in Figures 2b–2d). Additional simulations of moderately and strongly nonlinear shear waves (not shown) yield qualitatively similar cross-shore variations and agreement with observed phase speeds. The model results, and the close correspondence between C^u_{obs} and V_{obs} for the entire 4-month-long data set (shaded area in Figure 10b, from *Noyes et al.* [2004]) suggest that shear wave phase speeds often were determined by alongshore advection of eddies.

4.2. Magnitude of Velocity Fluctuations

[15] Observed and modeled frequency spectra have comparable levels and similar cross-shore structure at the dominant shear wave frequencies. For example, at 0.0022 Hz the observed and modeled spectral levels usually are within a factor of 2 near the shoreline, with similarly strong cross-shore decay (Figure 11). An exception is 13 November (Figure 11c), when the observed shear wave energy varies little over the cross shore. Although the numerical simulations deviate significantly from the most rapidly growing linear mode (the vertical scale of Figure 11 spans 3 decades), both exhibit strong cross-shore decay seaward of the surf zone. However, the model frequency spectra show a much steeper roll off at high frequencies than is observed (not shown, similar to *Özkan-Haller and Kirby* [1999]). This discrepancy is caused at least partially by neglected wave-current interactions [*Özkan-Haller and Li*, 2003].

[16] Root-mean-square (rms) shear wave flow speeds ($\langle u^2_{sw} \rangle^{1/2}$ and $\langle v^2_{sw} \rangle^{1/2}$) are estimated by integrating $E^{u,v}(k, f)$

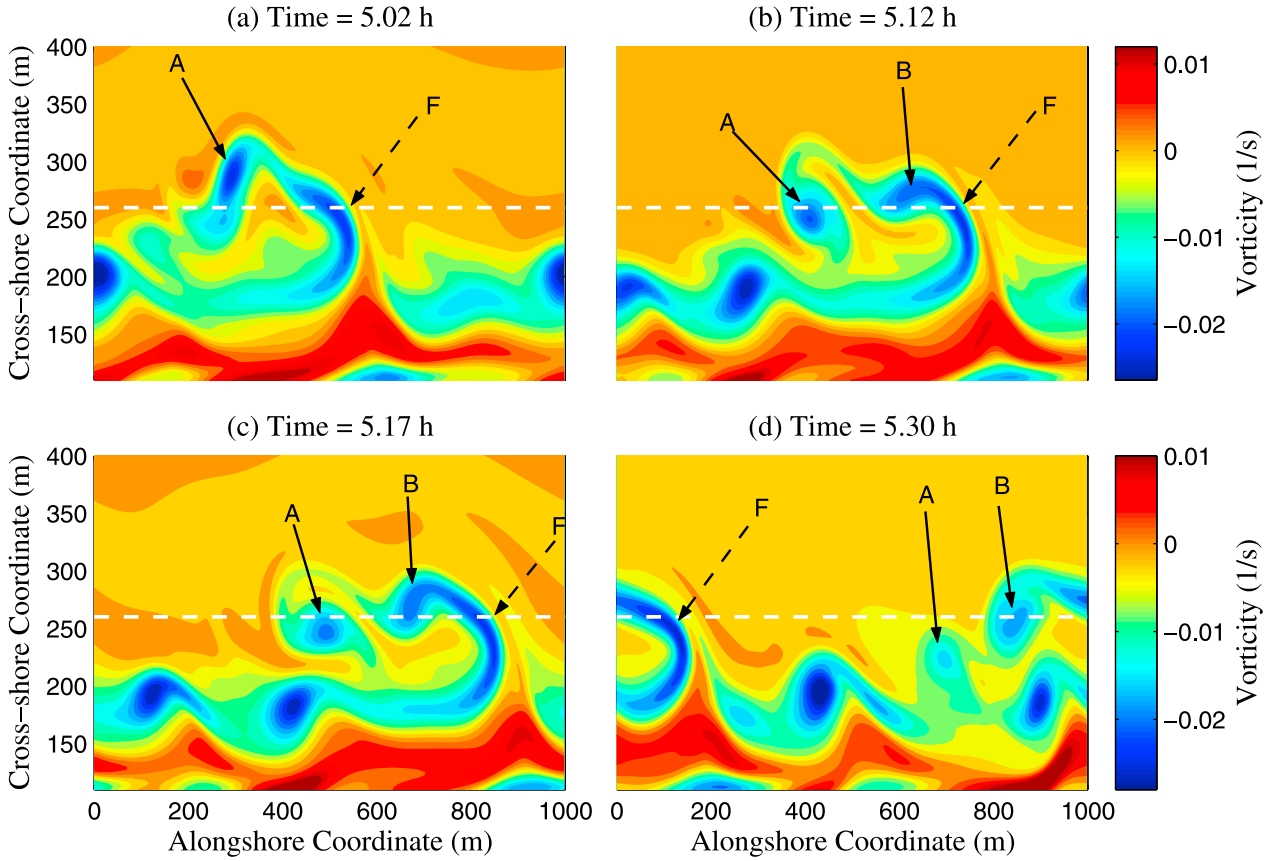

Figure 8. Numerically modeled vorticity (color scale to the right) on 1 November versus cross- and alongshore coordinates at times (a) 5.02 hours, (b) 5.12 hours, (c) 5.17 hours, and (d) 5.30 hours. The solid arrows indicate locations of eddies A and B. The dotted arrow labeled F indicates the vorticity front. All features propagate in the direction of the mean current (left to right), but the eddies propagate slower than the vorticity front. At array 3 (the cross-shore location of the vorticity time series shown in Figure 9, indicated here with a horizontal white dotted line) the alongshore separation between F and A increases from about 200 m at 5.02 h (Figure 8a) to about 300 m at 5.17 h (Figure 8c). The solutions are alongshore periodic, and thus F has wrapped around in Figure 8d, with F separated about 400 m from A.

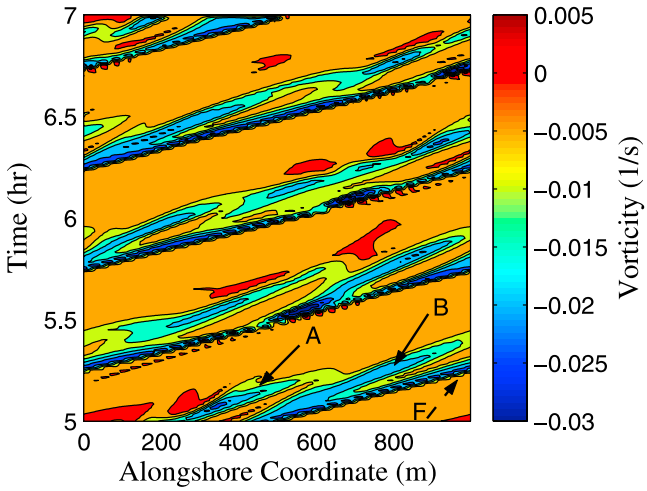

Figure 9. Numerically modeled vorticity (color scale is on the right) on 1 November at array 3 (cross-shore location x = 260 m) versus time t and alongshore coordinate y. The t-y trajectories of vorticity fronts are narrow, dark blue ridges with approximately constant slope corresponding to alongshore phase speed $C \approx 60$ cm/s. The front indicated with dashed arrow F (lower right-hand corner) also is labeled F in Figure 8. Eddies (solid arrows here and in Figure 8) propagate more slowly (≈40 cm/s, indicated by the slope of the light blue ridges) than the vorticity front. The formation of eddy B (see Figure 8) is indicated here by the emergence of light blue ridge B from the front F at $t \approx 5.0$ hours, $y \approx 500$ m. When eddy A drifts onshore of array 3 (see Figures 8c and 8d), the (light blue) ridge A terminates ($t \approx 5.2$ hours, $y \approx 550$ m).

over shear wave frequencies (0.00165–0.02500 Hz) and wave numbers (see, for data processing details, *Noyes et al.* [2004]). Underprediction at high frequencies and overprediction at low frequencies partially compensate, and observed and modeled shear wave rms flow speeds are within a factor of 2 on 1 November and 17 November (Figure 12), and within about a factor of 4 on 28 August and 13 November. In all four case examples the observed and predicted velocity variance is distributed roughly equally between the u and v components ($\langle u_{sw}^2 \rangle^{1/2} \approx \langle v_{sw}^2 \rangle^{1/2}$, Figure 12). This approximate isotropy of the shear wave velocity field was observed during the entire 4-month-long experiment [*Noyes et al.*, 2004], and in additional model simulations (not shown).

4.3. Rotary Flows

[17] Rotary spectra of the complex flow vector $u + iv$ give the energy of clockwise $S^+(f)$ and counterclockwise $S^-(f)$ rotating flow components as a function of frequency [*Gonella*, 1972]. The bulk (frequency-integrated) rotary coefficient, defined as

$$R_b = \frac{\int^{f_{max}} [S^+(f) - S^-(f)]\, df}{\int^{f_{max}} [S^+(f) + S^-(f)]\, df}, \qquad (1)$$

equals +1 (−1) for counterclockwise (clockwise) rotating velocity vectors with equal (and out of phase) u and v. If $R_b = 0$, there is no preferred sense of rotation. To prevent possible contamination by gravity motions in the observations at higher shear wave frequencies, f_{max} = 0.005 Hz. For each case example, R_b was computed using the numerical model and the currents observed along the central cross-shore transect (Figure 1). The observed and numerically modeled cross-shore variation of R_b agree qualitatively at locations where the observations are shear wave–dominated (compare solid curves with filled symbols in Figure 13). With the exception of the broad V on 13 November, the observed and modeled R_b change sign once across the surf zone. In contrast the linear stability R, based on the most rapidly growing linear eigenfunction, have multiple sign changes.

5. Summary

[18] Shear waves, instabilities of the breaking-wave-driven mean alongshore current (V), observed at 5 cross-

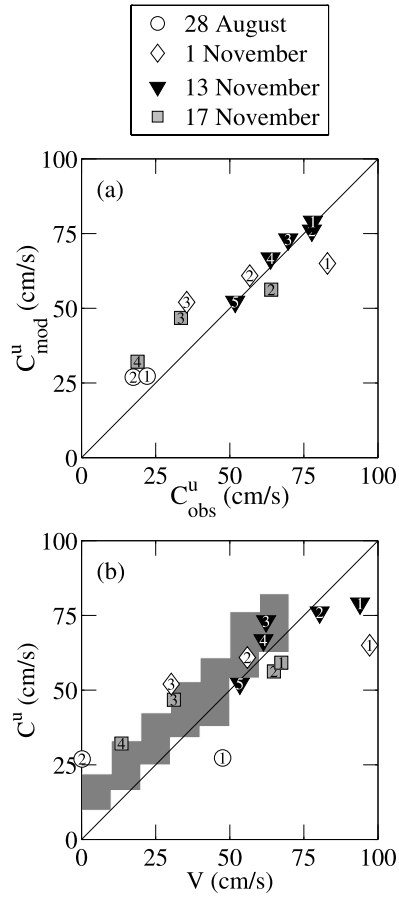

Figure 10. (a) Modeled C^u_{mod} versus observed C^u_{obs} shear wave phase speeds. Symbols correspond to different case examples (see legend), and the array number is indicated within each symbol. The solid line is $C^u_{mod} = C^u_{obs}$. (b) Phase speed C^u versus mean alongshore current V. Modeled case examples are shown as numbered symbols (see legend), and the plotted variables are $C_{mod}{}^u$ and V_{sw} (the solid line is $C^u_{mod} = V_{sw}$). Observations of C^u_{obs} and V_{obs} over the entire 4-month-long data set (mean ± one standard deviation [*Noyes et al.*, 2004]) are indicated by the shaded area (the solid line also corresponds to $C^u_{obs} = V_{obs}$).

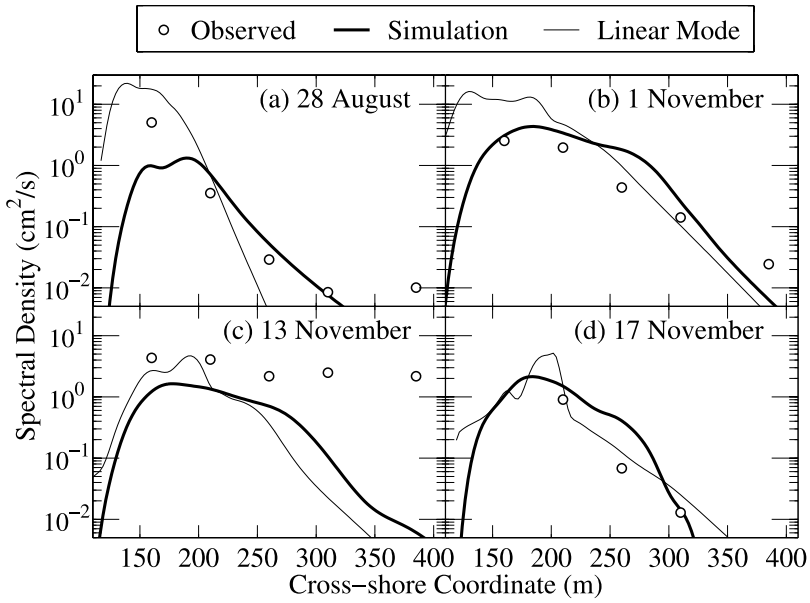

Figure 11. Observed (circles), numerically simulated (bold curves), and the linear mode (thin curves) of shear wave total (sum of cross- and alongshore) velocity spectral density at 0.0022 Hz versus cross-shore distance on (a) 28 August, (b) 1 November, (c) 13 November, and (d) 17 November. The linear mode amplitude is selected to match the numerically simulated value at array 2 (cross-shore coordinate x = 210 m).

shore locations between the shoreline and 5 m water depth were compared with numerical solutions of the nonlinear shallow water equations with wave forcing and bottom friction. Mean alongshore currents included a weak and a strong shoreline-intensified jet, a broad flow, and a strong mid-surf-zone jet. Wave forcing was estimated with a model for the shoaling and breaking of a narrowband wave field over the observed bathymetry, using fixed, standard values for adjustable model coefficients. The bottom drag coefficient for the nonlinear bottom stress in the circulation model, tuned to match the observed mean alongshore current V, is similar to previously estimated values. Modeled root-mean-square shear wave fluctuations are within a factor of about 3 of observed values.

[19] Close to shore, where V is strong and shear waves are energetic, observed and modeled shear wave alongshore phase speeds agree well, and are close to both the

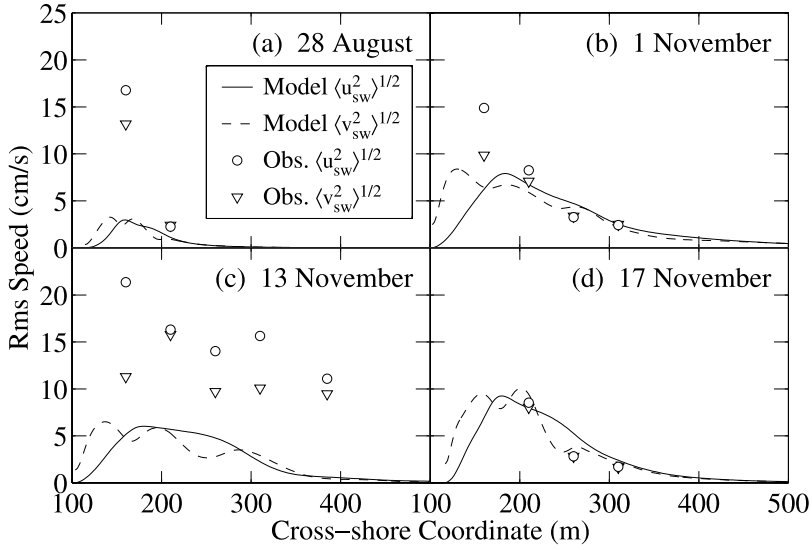

Figure 12. Observed (symbols) and numerically modeled (curves) cross- ($\langle u_{sw}{}^2\rangle^{1/2}$) and alongshore ($\langle v_{sw}{}^2\rangle^{1/2}$) rms shear wave velocity fluctuations versus cross-shore coordinate for (a) 28 August, (b) 1 November, (c) 12 November, and (d) 17 November.

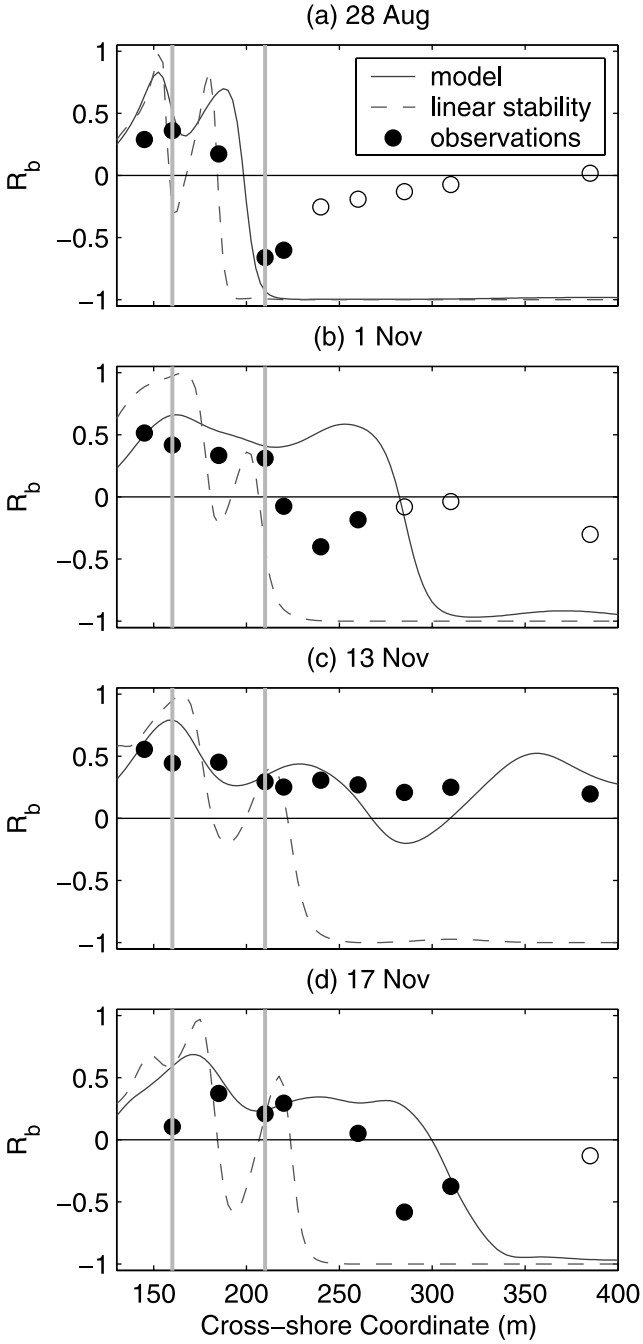

Figure 13. Bulk rotary coefficient R_b versus cross-shore coordinate for (a) 28 August, (b) 1 November, (c) 13 November, and (d) 17 November. Open circles indicate locations where the ratio of shear to gravity wave velocity variance is less than 3, suggesting contamination by gravity waves. Vertical shaded lines indicate the cross-shore locations of arrays 1 and 2. On 13 and 17 November (when V was directed southward) the sign of the rotary coefficient is reversed for comparison with the other cases.

local value of V and the phase speed of linearly unstable modes (as found by *Özkan-Haller and Kirby* [1999]). Farther offshore, where V is weak and shear wave energy levels are much reduced, both the observed and modeled alongshore phase speeds decrease to roughly the local V. A cross-shore decrease in the numerically simulated phase speed is consistent with the alongshore advection of eddies by the relatively weak and unsheared V offshore. The modeled cross- and alongshore shear wave velocity fluctuations have approximately equal magnitude, and the model velocity vectors change direction of rotation across the surf zone, similar to the observations.

Appendix A: Frequency-Directional Spectra

[20] At each alongshore array, velocity data collected at 2 Hz were processed in 3 hour segments that were quadratically detrended and divided into 448-s-long, demeaned, Hanning-windowed ensembles with 50% overlap. Cross spectra with about 24 degrees of freedom and 0.0011 Hz frequency resolution were used to estimate alongshore wave number–frequency spectra [$E^u(k, f)$ and $E^v(k, f)$] for cross- and alongshore (u, v) velocity components using the iterative maximum likelihood estimator (IMLE [*Pawka*, 1983]). Model $E(k, f)$ estimated using IMLE and a spatial array equivalent to the field array are similar to $E(k, f)$ estimated with a spatial FFT over the 1000-m-long model domain (phase speeds C from IMLE and FFT differ by less than 20%). Observed (IMLE) and modeled (FFT) shear wave $E(k, f)$ are shown here.

Appendix B: Model Summary

[21] Shear waves were modeled using the time-dependent, rigid-lid, nonlinear shallow water equations, averaged over incident wave timescales, and including forcing and dissipation, given by [*Allen et al.*, 1996; *Slinn et al.*, 1998]

$$\frac{\partial(hu)}{\partial x}+\frac{\partial(hv)}{\partial y}=0, \tag{B1a}$$

$$\frac{\partial(hu)}{\partial t}+\frac{\partial(hu^2)}{\partial x}+\frac{\partial(huv)}{\partial y}=-gh\frac{\partial\eta}{\partial x}-\frac{\tau_x^b}{\rho}-\nu h\nabla^4 u, \tag{B1b}$$

$$\frac{\partial(hv)}{\partial t}+\frac{\partial(huv)}{\partial x}+\frac{\partial hv^2}{\partial y}=-gh\frac{\partial\eta}{\partial y}+F_y-\frac{\tau_y^b}{\rho}-\nu h\nabla^4 v, \tag{B1c}$$

where (x, y) and (u, v) are the cross- and alongshore coordinates and velocities, respectively, t is time, η is the free surface, g is gravity, ρ is density, and ν is viscosity. Alongshore homogeneous bathymetry $h(x)$ and incident waves are assumed. Alongshore forcing F_y is the sum of the alongshore wind stress τ^{wind} and wave forcing dS_{yx}/dx:

$$F_y=\rho^{-1}\left(\tau_y^{\text{wind}}+\frac{dS_{yx}}{dx}\right). \tag{B2}$$

Bottom stress (τ_x^b and τ_y^b) is given by a quadratic stress law

$$\tau_x^b=\rho c_d\langle|\mathbf{u}|u\rangle \tag{B3a}$$

$$\tau_y^b=\rho c_d\langle|\mathbf{u}|v\rangle, \tag{B3b}$$

where c_d is a nondimensional drag coefficient, $\langle\ \rangle$ indicates averaging over incident wave timescales, and u and v contain incident velocity fluctuations given by the wave transformation model (Appendix C), shear waves, and the mean flow. The averages are evaluated at each time step using the formulation of *Ebersole and Dalyrmple* [1980] (an accurate approximation of $\langle|\mathbf{u}|v\rangle$ in field conditions [*Feddersen et al.*, 2000]). Biharmonic friction (i.e., $\nu h\nabla^4 u$, with hyperviscosity ν of $O(1\ m^4/s)$) is included to suppress numerical instabilities at high wave numbers, and is important primarily at the shoreline.

[22] The alongshore boundary conditions are periodic, and the cross-shore boundary conditions are

$$hu = u_{xx} = v_x = v_{xxx} = 0 \quad \text{at} \quad x = 0,\ L_x, \tag{B4}$$

where subscripts indicate differentiation with respect to that variable. The nonlinear shallow water equations (B1) are initialized with a frictionally balanced alongshore current (i.e., $F_y = \tau_y^b/\rho - \nu h\nabla^4 v$), and perturbed with a small (1 cm/s) amplitude, fastest growing linearly unstable mode of $V(x)$.

[23] Equations (B2)–(B4) are time stepped using a second-order Adams-Bashforth algorithm, and solved on a spatially uniform ($dx = dy = 2.5$ m), staggered C grid that spans cross-shore distance $L_x = 600$ m and alongshore distance $L_y = 1000$ m (4–8 alongshore wavelengths of the fastest-growing mode of $V(x)$). The averages (B3) are evaluated at each time step. The free surface is derived from a direct Poisson solver. Shear instabilities grew to finite amplitude and stabilized within 4 hours, and the time series of the next 4 hours of the model simulations were analyzed.

Appendix C: Wave Transformation Model

[24] A wave transformation model was used to estimate incident wave forcing dS_{yx}/dx (B4) (see, for details and references, *Ruessink et al.* [2001]). Breaking wave energy is transferred to a roller, delaying the transfer of breaking incident wave momentum to the mean flow. The radiation stress is given by

$$S_{yx} = \frac{1}{2}\ E_w\ \frac{c_g}{c}\sin 2\theta + E_r \sin 2\theta, \tag{C1}$$

where c and c_g are the incident wave phase and group speeds, $E_w = (1/8)\ \rho g H_{\text{rms}}^2$ and E_r are the incident wave and roller energy, and H_{rms} is the root-mean-square wave height. The incident waves are assumed stationary, and narrow in frequency and direction θ. The (energy-weighted) mean frequency f_m of the frequency spectrum $E(f)$ in 8 m water depth was used to estimate c and c_g. Cross-shore changes in θ are given by Snell's law, with an offshore incident wave angle θ_{inc} determined from (C1) using the total (frequency-integrated) E_w and S_{yx} observed in 8 m water depth and $E_r = 0$. Evolution equations for E_w and E_r are

$$\frac{d}{dx}\left(E_w c_g \cos\theta\right) = \epsilon_w, \tag{C2a}$$

$$\frac{d}{dx}\left(E_r c \cos\theta\right) = \epsilon_r - \epsilon_w, \tag{C2b}$$

with dissipations

$$\epsilon_w = -\frac{1}{4} Q f_m \rho g H_m^2 \qquad \epsilon_r = -\frac{2 g E_r \sin\beta}{c},$$

where

$$H_m = \frac{0.88}{k_m}\tanh\left(\frac{\gamma k_m h}{0.88}\right), \quad \gamma = 0.5 + 0.5\tanh(33s),$$

and s is the deep water wave steepness. The wave number k_m of the incident waves is determined from h and f_m using the linear finite depth dispersion relationship. The wave height parameters (H_{rms} and H_m) and the fraction of breaking waves (Q) are related by

$$\frac{1-Q}{-\ln Q} = \frac{H_{\text{rms}}^2}{H_m^2}, \tag{C3}$$

where the wave heights H are Rayleigh-distributed up to the cutoff $H = H_m$ [*Battjes and Stive*, 1985]. Integration of (C2) from 8 m water depth shoreward using one-sided finite differences yields the cross-shore distribution of E_w and E_r. As the roller parameter β decreases, the roller dissipation rate decreases and the location of maximum dS_{yx}/dx is displaced farther shoreward. In all runs, $\beta = 0.1$, similar to previously used values [*Walstra et al.*, 1996; *Ruessink et al.*, 2001]. Agreement between the observed and modeled (including shear waves) V usually is improved by including a roller (not shown).

[25] On 1 and 17 November, and other days with strong, shoreline-intensified jets (not shown) unphysically large, wave-driven V were predicted within 40 m of the shoreline. These could be suppressed by using a drag coefficient that increases in shallow water [*Ruessink et al.*, 2001], or by altering the nearshore bathymetry. Instead, cubic spline smoothing was used to produce wave-driven V with shoreline values similar to model values about 50 m from the shoreline (Figures 2b and 2c).

[26] **Acknowledgments.** This research was supported by the Office of Naval Research, the National Oceanographic Partnership Program, and the National Science Foundation. The nearshore arrays were deployed and maintained by staff from the Center for Coastal Studies, Scripps Institution of Oceanography. Staff from the U.S. Army Corps of Engineers Field Research Facility, Duck, North Carolina, provided processed survey data, data from their pressure array in 8 m water depth, and excellent logistical support. We thank Britt Raubenheimer for contributions to the field experiment.

References

Allen, J. S., P. A. Newberger, and R. A. Holman (1996), Nonlinear shear instabilities of alongshore currents on plane beaches, *J. Fluid. Mech.*, *310*, 181–213.

Battjes, J. A., and M. J. F. Stive (1985), Calibration and verification of a dissipation model for random breaking waves, *J. Geophys. Res.*, *90*, 9159–9167.

Bowen, A. J., and R. A. Holman (1989), Shear instabilities of the mean longshore current: 1. Theory, *J. Geophys. Res.*, *94*, 18,023–18,030.

Church, J. C., and E. B. Thornton (1993), Effects of breaking wave induced turbulence within a longshore current model, *Coastal Eng.*, *20*, 1–28.

Dodd, N., J. Oltman-Shay, and E. B. Thornton (1992), Shear instabilities in the longshore current: A comparison of observations and theory, *J. Phys. Oceanogr.*, *22*, 62–82.

Dodd, N., V. Iranzo, and A. Reniers (2000), Shear instabilities of wave-driven alongshore currents, *Rev. Geophys.*, *38*, 437–464.

Ebersole, B. A., and R. A. Dalyrmple (1980), Numerical modeling of nearshore circulation, in *Proceedings of the 17th Internationl Coastal*

Engineering Conference, pp. 2710–2725, Am. Soc. of Civ. Eng., New York.

Feddersen, F. (1998), Weakly nonlinear shear waves, *J. Fluid. Mech.*, *372*, 71–92.

Feddersen, F., and R. T. Guza (2003), Observations of nearshore circulation: Alongshore uniformity, *J. Geophys. Res.*, *108*(C1), 3006, doi:10.1029/2001JC001293.

Feddersen, F., R. T. Guza, S. Elgar, and T. H. C. Herbers (2000), Velocity moments in alongshore bottom stress parameterizations, *J. Geophys. Res.*, *105*, 8673–8686.

Feddersen, F., R. T. Guza, and S. Elgar (2004), Inverse modeling of one-dimensional setup and alongshore currents in the nearshore, *J. Phys. Oceanogr.*, *34*, 920–933.

Gonella, J. (1972), A rotary-component method for analyzing meteorological and oceanographic time series, *Deep Sea Res.*, *19*, 833–846.

Haller, M. C., U. Putrevu, J. Oltman-Shay, and R. A. Dalrymple (1999), Wave group forcing of low frequency surf zone motion, *Coastal Eng. J.*, *41*, 121–136.

Long, C. E. (1996), Index and bulk parameters for frequency-direction spectra measured at CERC Field Research Facility, June 1994 to August 1995, *Misc. Pap. CERC-96-6*, U.S. Army Eng. Waterw. Exper. Stn., Vicksburg, Miss.

Noyes, T. J., R. T. Guza, S. Elgar, and T. H. C. Herbers (2004), Field observations of shear waves in the surf zone, *J. Geophys. Res.*, *109*, C01031, doi:10.1029/2002JC001761.

Oltman-Shay, J., P. A. Howd, and W. A. Birkemeier (1989), Shear instabilities of the mean longshore current: 2. Field observations, *J. Geophys. Res.*, *94*, 18,031–18,042.

Özkan-Haller, H. T., and J. T. Kirby (1999), Nonlinear evolution of shear instabilities of the longshore current: A comparison of observations and computations, *J. Geophys. Res.*, *104*, 25,953–25,984.

Özkan-Haller, H. T., and Y. Li (2003), Effects of wave-current interaction on shear instabilities of longshore currents, *J. Geophys. Res.*, *108*(C5), 3139, doi:10.1029/2001JC001287.

Pawka, S. (1983), Island shadows in wave directional spectra, *J. Geophys. Res.*, *88*, 2579–2591.

Ruessink, B. G., J. R. Miles, F. Feddersen, R. T. Guza, and S. Elgar (2001), Modeling the alongshore current on barred beaches, *J. Geophys. Res.*, *106*, 22,451–22,463.

Slinn, D. N., J. S. Allen, P. A. Newberger, and R. A. Holman (1998), Nonlinear shear instabilities of alongshore currents over barred beaches, *J. Geophys. Res.*, *103*, 18,357–18,379.

Svendsen, I. A., and U. Putrevu (1994), Nearshore mixing and dispersion, *Proc. R. Soc. London, Ser. A*, *445*, 561–576.

Walstra, D. J. R., G. P. Mocke, and F. Smit (1996), Roller contributions as inferred from inverse modeling techniques, in *Proceedings of the 25th International Coastal Engineering Conference*, pp. 1205–1218, Am. Soc. of Civ. Eng., New York.

S. Elgar, Woods Hole Oceanographic Institution, Woods Hole, MA 02543, USA. (elgar@whoi.edu)

F. Feddersen, R. T. Guza, and T. J. Noyes, Integrative Oceanography Division, Scripps Institution of Oceanography, 9500 Gilman Drive 0209, La Jolla, CA 92093-0209, USA. (ffeddersen@ucsd.edu; rguza@ucsd.edu; tnoyes@elcamino.edu)

T. H. C. Herbers, Department of Oceanography, Code OC/He, Naval Postgraduate School, Monterey, CA 93943-5122, USA. (herbers@oc.nps.navy.mil)